SHIRMS 2008 – Y. Potvin, J. Carter, A. Dyskin, R. Jeffrey (eds)
© 2008 Australian Centre for Geomechanics, Perth, ISBN 978-0-9804185-5-2
doi:10.36487/ACG_repo/808_107

Modelling Pore Pressure/Stress Coupling

B.I.R. Müller *Karlsruhe University, Germany*

J.B. Altmann *Karlsruhe University, Germany*

A. Dorner *Karlsruhe University, Germany*

T.M. Müller *Karlsruhe University, Germany*

M.R.P. Tingay *Adelaide University, Australia*

Abstract

Time-dependent changes of pore pressure due to injection into, or depletion from, reservoirs cause a spatial-temporal redistribution of stress in and around the reservoirs. Reservoirs are complex underground storage volumes in which predictions of four-dimensional (4D) variations of pore pressure/stress can be achieved by geomechanical modelling. Poroelastic modelling takes into account the coupling of pore pressure and stress. To quantify the spatial-temporal evolution of pore pressure/stress coupling in complex settings we solve the coupled differential equations of quasi-static poroelasticity with the three-dimensional (3D) finite element method. For simple settings our modelling tool matches the analytical description of pore pressure/stress values. We show that, for the long-term limit, the analytical solutions approach the static limit, which is derived for uniaxial strain conditions. Our modelling results indicate that in the early stage of fluid injection experiments pore pressure/stress coupling deviates significantly from the static limit. This implies that the range of observed pore pressure/stress coupling values may arise from the fact that some values have been measured in reservoirs that have not reached the static conditions yet. Furthermore, our results indicate strong increases of pore pressure/stress coupling ratios at the reservoir boundaries.

1 Introduction

Depletion of reservoirs causes deformation processes and stress changes within the reservoir and in its surroundings. Repeated measurements of stress and pore pressure P during the depletion of oil fields show that changes in P and minimum horizontal stress σ_h are coupled to one another, which is called pore pressure/stress coupling (Hillis, 2000). These changes affect physical parameters such as acoustic-wave velocity, bulk density, porosity and permeability that may lead to modifications of reservoir fluid flow, reactivation of reservoir-sealing faults, failure of the caprock or induced microseismicity, phenomena that have profound impact on reservoir management. Predictive geomechanical modelling of reservoir response on depletion or injection processes is an essential tool to forecast fluid flow and stress change.

Analytical solutions to describe the spatial-temporal redistribution of P and stress using linear poroelasticity have been derived for simple geometries (Geertsma, 1973; Rudnicki, 1986; Segall, 1992; Wang, 2000). Numerical models with uniform prescribed depletion of P show that part of the weight of the overburden is transferred to the formations at the sides of the reservoir (stress arching), leading to higher risk for failure (Mulders, 2003; Roest et al., 1999). In general, reservoirs are complex storage volumes and geological systems such as fields of mud volcanoes or overpressured segments of reservoirs show that P is not homogeneously distributed. To quantify the spatial-temporal evolution of pore pressure/stress coupling in complex tectonic settings due to injection/depletion into the reservoir we solve the coupled differential equations of poroelasticity with the 3D finite element method. Our results indicate that in the early stage of fluid injection/depletion pore pressure/stress coupling deviates from the static value. We show theoretically, that the static value is the long-term limit of point injection, which explains the observed variability of pore pressure/stress coupling ratios.

2 Observations and implications from depletion-induced microseismicity and pore pressure/stress coupling

Using Terzaghi´s effective stress concept and P independent stresses in a Mohr–Coulomb failure criterion one would expect that depletion of a reservoir results into a decreasing probability of rock failure, thus it would enhance stability. However, the observation of depletion-induced microseismicity, as reported by numerous authors (Grasso, 1992; Rutledge et al., 1998; van Eck et al., 2006) contradicts this description and motivates the concept of pore pressure/stress coupling (Engelder and Fischer, 1994; Hillis, 2000, 2001; 2003), which is briefly described in the following and which can be predicted by poroelasticity.

2.1 Depletion-induced microseismicity

Depletion-induced seismicity due to oil and gas production became a growing problem in numerous fields world-wide, for example in Texas (Yerkes and Castle, 1976), the Oman (Sze et al., 2005), Canada (Mereu et al., 1986), the North Sea (Teufel, 1996; Teufel et al., 1991), France (Grasso and Wittlinger, 1990), or the Permian basin (Doser et al., 1992). According to (Rutledge et al., 1998) the seismic behaviour of the Seventy-six oil field in Clinton county Kentucky reflects an increase in horizontal compression above and below the drained volumes. In Europe, most pronounced depletion related seismicity is reported from the Netherlands (van Eijs et al., 2006) and the Lacq field in France (Grasso and Wittlinger, 1990; Feigner and Grasso, 1990). Earthquakes related to massive fluid or gas extraction fall in three categories:

- Shallow M_L 5 seismic instabilities above or below the producing formation, that typically exhibit normal or reverse faulting focal mechanism and may be associated with the rapid subsidence and poroelastic strain changes (Grasso, 1992; Nicholson and Wesson, 1992).
- Earthquakes within the producing horizons, that mostly occur along pre-existing (sealing) faults and have magnitudes of M_L ca. 4. (van Eck et al., 2006; Dost and Haak, 2007).
- Deep earthquakes, that often exhibit thrust mechanism and $M_L > 6$ and may be related to stress and strain changes associates with unloading effects (McGarr, 1982; Simpson and Leith, 1985). Here we consider changes of the stress pattern within the reservoir and its immediate vicinity.

2.2 Pore pressure/stress coupling – observations

Repeated measurements of pore pressure and horizontal stress within sedimentary basins world-wide provide evidence for the coupling of changes in pore pressure to changes in total minimum horizontal stress magnitude (Hillis, 2000; 2001). Depletion-induced reduction in pore pressure P in hydrocarbon reservoirs leads to a decrease of the total minimum horizontal stress magnitude σ_h; conversely, an increase of the total minimum horizontal stress magnitude is observed in overpressured zones of sedimentary basins (Tingay et al., 2003). This phenomenon is called pore pressure/stress coupling or also known as stress depletion response of the reservoir (Addis, 1997). Pore pressure/stress coupling affect the stability of wellbores and has significant implications for fluid flow in sedimentary basins. Tingay et al., (2003) differentiate between basin-scale pore pressure/stress coupling, that has been demonstrated in the Scotian Shelf (Bell, 1990; Ervine and Bell, 1987) or Brunei (Tingay et al., 2003) and field-scale pore pressure/stress coupling, where the relationship is observed to occur over a time scale of years during the depletion of a reservoir. Examples for field-scale pore pressure/stress coupling can be found in reservoirs in Texas (Salz, 1977), Venezuela (Breckels and van Eekelen, 1982) or the Ekofisk–Field in the North Sea (Teufel et al., 1991). The average of the measured pore pressure/stress coupling ratios is $\Delta\sigma_h/\Delta P = 64\%$ (Table 1). But, as shown in Table 1 there is a rather high variability in the pore pressure/stress coupling ratios. The minimum value is 0.34 and the maximum value is 1.18. We will show that this variability can be interpreted as a result from a time-dependent inhomogeneous distribution of P and stress.

Table 1 Basin and field scale values for the pore pressure/stress coupling ratio $\Delta\sigma_h/\Delta P$. This compilation is based on (Hillis, 2000) and Tingay (pers. communication). The average value is 64%

Area	Scale	$\Delta\sigma_h/\Delta P$
Scotian shelf, Canada	Overpressured basin	0.76
North West shelf, Australia	Overpressured basin	0.75
Gannet and Guillemot fields, North Sea	Overpressured basin	0.60
Vicksburg formation, South Texas	Depletion in field	0.48
Travis Peak formation, East Texas	Depletion in field	0.57
Alberta basin, Western Canada	Depletion in field	0.34
Ekofisk field, North Sea	Depletion in field	~0.8
US Gulf Coast	Depletion in field and overpressured basin	0.46
Lake Maracaibo, Venezuela	Depletion in field	0.56
Baram Delta Province, Brunei	Depletion in field and overpressured basin	0.59
Magnus field, North Sea	Depletion in field	0.68
West Sole field, North Sea	Depletion in field	1.18
Wytch Farm field, UK	Depletion in field	0.65
Venture field, Canada	Overpressured basin	0.56
Nile Delta, Egypt	Overpressured basin	0.65

2.3 Pore pressure/stress coupling implications

For reactivation of reservoir-bounding faults or for seismicity, it is the effective normal stress that controls the resistance to slip. This is manifested using the classical approach with Terzaghi´s model, where stresses are independent of pore pressure P and effective vertical, maximum and minimum horizontal stresses are defined by $\sigma_{veff} = \sigma_v - P$, $\sigma_{Heff} = \sigma_H - P$, $\sigma_{heff} = \sigma_h - P$ (please note that we use the sign convention where compression is positive) in combination with a modified Coulomb criterion:

$$\tau = \mu(\sigma_n - P) + C \tag{1}$$

τ and σ_n are the shear and normal stresses on the failure plane, C is the cohesion and μ is the coefficient of static friction. An increase of P leads to a reduction of the resistant effective normal stress and thus destabilises a fault. This can be illustrated with Mohr circles. Figures 1 and 2 illustrate the example of a normal faulting regime with $\sigma_1 = \sigma_v$, $\sigma_2 = \sigma_H$, $\sigma_3 = \sigma_h$ and $\sigma_{1eff} = \sigma_v - P$, $\sigma_{2eff} = \sigma_H - P$, $\sigma_{3eff} = \sigma_h - P$.

For pressure-independent stresses an increase in pore pressure leads to a reduction of effective stresses σ_{veff} and σ_{heff} at the same rate. This results in a shift of the Mohr circle to the left approaching the failure envelope which would destabilise faults in reservoirs. Conversely, a decrease in pore pressure, such as depletion, would stabilise faults.

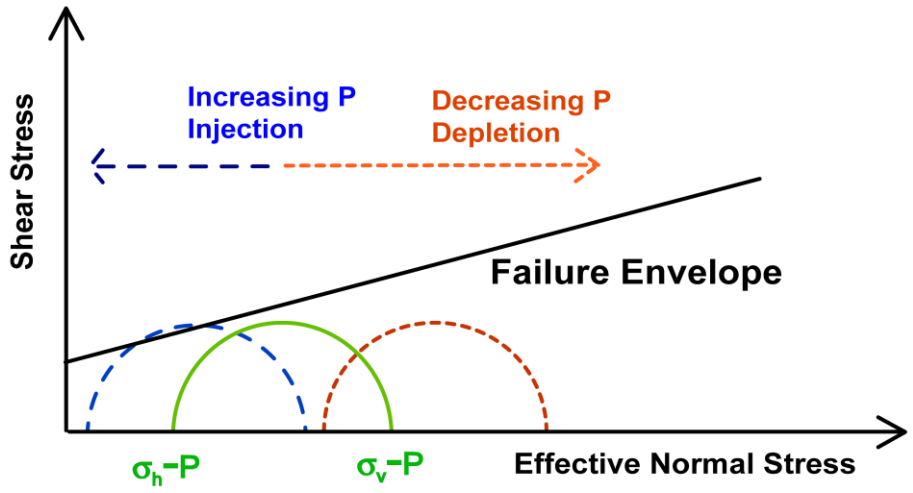

Figure 1 **Conventional models with pressure-independent total stresses predict destabilisation in case of increasing pore pressure ΔP > 0, injection) because the Mohr circles shift to the left, closer to the failure envelope and stabilisation for decreasing pore pressure (ΔP < 0, depletion)**

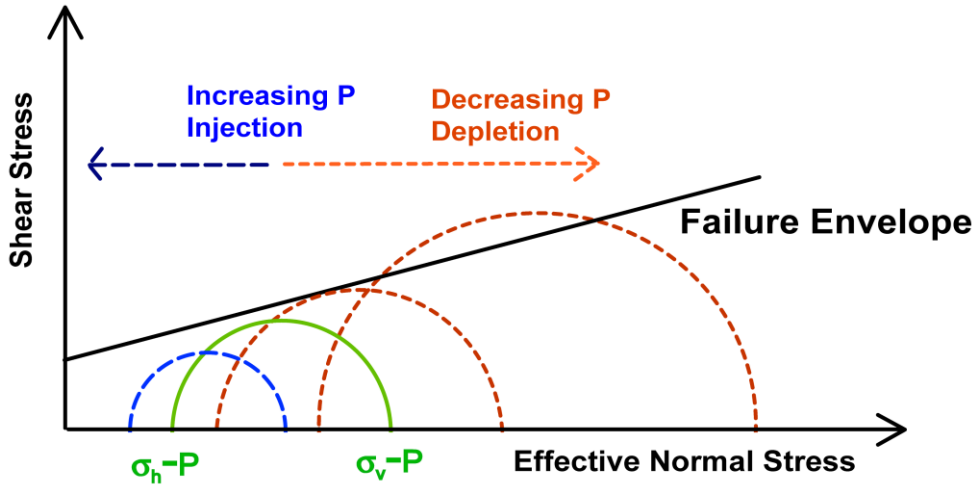

Figure 2 **Pore pressure/stress coupling generates for decreasing P (depletion) a reduction of the total minimum horizontal stress and therefore the effective horizontal stress increases less than the effective vertical stress which leads to an increase of the Mohr circle and higher risk to reach the failure envelope. In the case of injection the size of the Mohr circle is reduced, since the effective horizontal stress is reduced less than the effective vertical stress**

However, as described previously, microseismicity is also associated with reservoir depletion. The observed ratios of pore pressure/stress coupling can be used to understand brittle failure in depleting reservoirs. If the horizontal stress is coupled to the pore pressure by a 64% pore pressure/stress coupling value, then the total minimum horizontal stress σ_h is decreased to $\sigma_h = \sigma_{h0} + 0.64\Delta P$ during depletion (ΔP < 0), because $\Delta\sigma_h = \sigma_h - \sigma_{h0} = 0.64\Delta P$ is less than zero. The change of horizontal effective stress is then $\Delta\sigma_{heff} = 0.64\Delta P - \Delta P$, whereas the change in vertical effective stress is $\Delta\sigma_{veff} = -\Delta P$. This leads to a greater differential effective stress and thus to an enlargement of the Mohr circle which may result in reaching the failure envelope (Figure 2). During injection, the total horizontal stress increases by 64% of ΔP and thus, the effective horizontal stress is reduced less than the vertical effective stress. This leads to a reduction of differential stress and therefore to a smaller Mohr circle. In this case, fluid-injection into a reservoir can stabilise a fault.

3 Static and spatial-temporal concepts of pore pressure/stress coupling

The nature of pore pressure/stress coupling was investigated by numerous authors, for example (Engelder and Fischer, 1994) and (Hillis, 2001). To describe the observed phenomenon of pore pressure/stress coupling Engelder and Fischer (1994) derived a relation between the changes in horizontal stress and pore pressure for horizontally extending reservoirs under static and uniaxial strain conditions.

Under the assumptions that the vertical stress magnitude is constant and can be derived from the weight of the overburden at depth z and that under uniaxial strain conditions the vertical stress and minimum horizontal stress are related by $\sigma_h = \nu/(1 - \nu)\sigma_v$, Engelder and Fischer (1994) obtain an empirical relationship for the pore pressure/stress coupling ratio $\Delta\sigma_h/\Delta P$:

$$\frac{\Delta\sigma_h}{\Delta P} = \zeta\frac{1-2\nu}{1-\nu} \tag{2}$$

Assuming typical values for the Biot–Willis coefficient $\zeta \approx 1$ and the Poisson's ratio $\nu = 0.25$ yields $\Delta\sigma_h/\Delta P = 0.66$. This value agrees well with the observed average value of $\Delta\sigma_h/\Delta P$. This result is based on a homogeneous pore pressure change within a laterally extending reservoir. It does not contain a time dependence of pore pressure/stress coupling and thus represents a static approach.

To obtain the spatial-temporal variation of pore pressure/stress coupling we use analytical expressions for the temporal and spatial distributions of pore pressure/stress tensor components due to a continuous fluid injection (or depletion) at a point in an infinite homogeneous poroelastic medium (Rudnicki, 1986; Wang, 2000):

$$p(\mathbf{x},t) = \frac{\mathrm{q}}{\rho_0 \mathrm{c}}\frac{1}{4\pi r}\left[\frac{(\lambda_\mathrm{u}-\lambda)(\lambda+2\mu)}{\zeta^2(\lambda_\mathrm{u}+2\mu)}\right]\mathrm{erfc}\left(\frac{1}{2}\xi\right) \tag{3}$$

$$\sigma_{ij}(\mathbf{x},t) = \frac{\mathrm{q}}{\rho_0 \mathrm{c}}\frac{(\lambda_\mathrm{u}-\lambda)\mu}{4\pi r\zeta(\lambda_\mathrm{u}+2\mu)} \left\{\delta_{ij}\left[\mathrm{erfc}\left(\frac{1}{2}\xi\right) - 2\xi^{-2}\mathrm{g}(\xi)\right] + \left(\mathrm{x_i x_j}/r^2\right)\left[\mathrm{erfc}\left(\frac{1}{2}\xi\right) + 6\xi^{-2}\mathrm{g}(\xi)\right]\right\} \tag{4}$$

where q represents a constant-rate fluid mass source, ρ_0 fluid density, $\xi = r/\sqrt{ct}$ is the Boltzmann variable and c the diffusivity. The Lamé parameters under drained conditions are λ and μ, whereas the undrained Lamé parameter is λ_u. The Biot–Willis coefficient is denoted as $\zeta = 1 - K/K_s$, where K is the drained bulk modulus and K_s is the bulk modulus of the solid constituents. The distance between pressure source (for injection (q > 0) or depletion (q < 0)) and observation point is **x**. In Equations (3) and (4) we use the function:

$$g(\xi) = \left(2\pi^{1/2}\right)^{-1}\int_0^\xi s^2\,\mathbf{exp}\left(-\frac{1}{4}s^2\right)ds = erf\left(\frac{1}{2}\xi\right) - \pi^{-1/2}\xi\,\mathbf{exp}\left(-\frac{1}{4}\xi^2\right) \tag{5}$$

where erfc denotes the complementary error function.

The pore pressure/stress coupling value as a function of time since the beginning of injection (or depletion) is given by:

$$\frac{\Delta\sigma_{ij}(\mathbf{x},t)}{\Delta p(\mathbf{x},t)} = \frac{\frac{q}{\rho_0 c}\frac{(\lambda_u-\lambda)\mu}{4\pi r\zeta(\lambda_u+2\mu)}\left\{\delta_{ij}\left[\operatorname{erfc}\left(\frac{1}{2}\xi\right)-2\xi^{-2}g(\xi)\right]+\left(x_i x_j/r^2\right)\left[\operatorname{erfc}\left(\frac{1}{2}\xi\right)+6\xi^{-2}g(\xi)\right]\right\}}{\frac{q}{\rho_0 c}\frac{1}{4\pi r}\left[\frac{(\lambda_u-\lambda)(\lambda+2\mu)}{\zeta^2(\lambda_u+2\mu)}\right]\operatorname{erfc}\left(\frac{1}{2}\xi\right)} \tag{6}$$

Here, it is possible to introduce the formulas of (Rudnicki, 1986) since initially P(x,t) = 0 and $\sigma_{ij}(x,t)$. For any radial stress component, thus also the horizontal stress component, Equation (6) simplifies to:

$$\frac{\Delta\sigma_h(r,t)}{\Delta p(r,t)} = \frac{\left\{\left[\operatorname{erfc}\left(\frac{1}{2}\xi\right)-2\xi^{-2}g(\xi)\right]+\left[\operatorname{erfc}\left(\frac{1}{2}\xi\right)+6\xi^{-2}g(\xi)\right]\right\}}{\left[\frac{(\lambda+2\mu)}{\zeta\,\mu}\right]\operatorname{erfc}\left(\frac{1}{2}\xi\right)}$$

$$\frac{\Delta\sigma_h(r,t)}{\Delta p(r,t)} = \frac{\left\{\left[2\operatorname{erfc}\left(\frac{1}{2}\xi\right)+4\xi^{-2}g(\xi)\right]\right\}}{\left[\frac{(\lambda+2\mu)}{\zeta\,\mu}\right]\operatorname{erfc}\left(\frac{1}{2}\xi\right)} = 2\frac{\zeta\,\mu}{(\lambda+2\mu)}\left\{1+\frac{2\xi^{-2}g(\xi)}{\operatorname{erfc}\left(\frac{1}{2}\xi\right)}\right\} \tag{7}$$

Since $\frac{\mu}{(\lambda+2\mu)} = \frac{1-2\nu}{1-\nu}$ according to (Jaeger and Cook, 1979), the difference between the time-dependent pore pressure/stress coupling ratio and Engelder´s static solution depends on the spatial-temporal contribution of the second summand. It is shown in the appendix, that for $\xi \to 0$, which represents either a zero distance to the injection or an infinite injection time t:

$$\lim_{t\to\infty}\frac{2\cdot g(\xi)}{\xi^2\cdot erfc\left(\frac{1}{2}\xi\right)} = 0 \tag{8}$$

Therefore, the pore pressure/stress coupling ratio for infinite injection times is calculated as limiting value:

$$\lim_{t\to\infty}\frac{\sigma_h(\mathbf{x},t)}{p(\mathbf{x},t)} = \zeta\frac{1-2\nu}{1-\nu} \tag{9}$$

This demonstrates that the pore pressure/stress coupling ratio based on the poroelastic relationships of (Rudnicki, 1986) passes into Equation (2) if time tends to infinity. Equation (2) is therefore the static limit for pore pressure/stress coupling in reservoirs for the smaller horizontal stress. Since we used the approach of a point injection into a homogeneous reservoir, this relationship would also hold for the maximum horizontal and the vertical stress components, whereas the relationship of Equation (2) by Engelder and Fischer (1994) has been derived under uniaxial strain conditions and constant vertical stress.

4 Modelling the spatial-temporal evolution of pore pressure/stress coupling

In order to investigate the spatial-temporal evolution of pore pressure and horizontal stress, we developed a 3D numerical model both for a homogeneous medium and for an inhomogeneous medium representing a

reservoir as specified in Figure 3. The results of the finite-element simulation using the numerical solver Abaqus are compared with the analytical solutions for P and σ_h given by Equations (3) and (4).

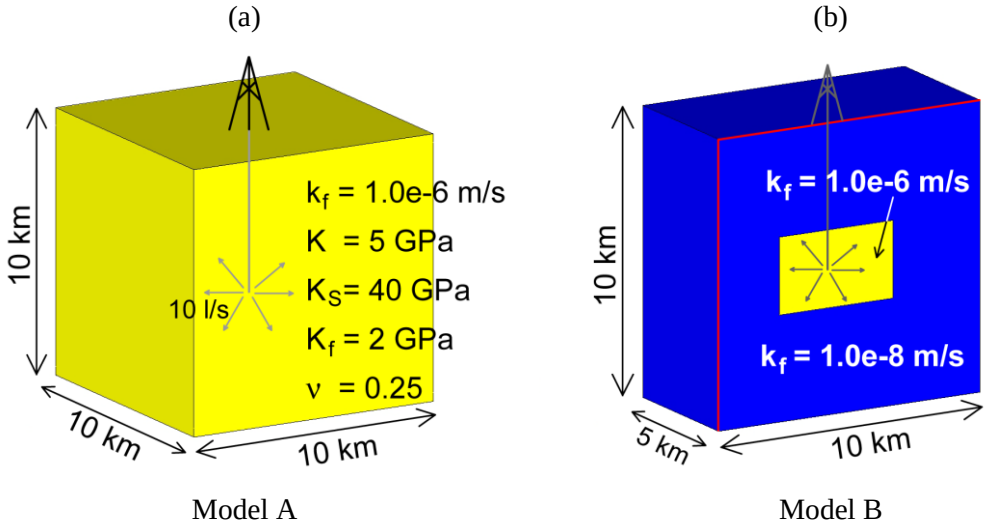

Figure 3 Two models with poroelastic rheology: (a) Homogeneous medium with fluid injection near the model centre (Model A). Element size is 300 m in x, y, z directions. Zero horizontal strain at the lateral boundaries is imposed; (b) A high-permeability region (reservoir) embedded in a homogenous background (Model B)

Model A is a homogeneous model with injection close to the model centre (Figure 3(a)) and with undrained model boundaries. The numerical results for P match with the analytical solutions, especially for shorter injection times (Figure 4). The ratio $\Delta\sigma_h/\Delta P$ reasonably matches with the analytical solutions (Figure 5). The deviations might be attributed to the finite size of the model and the undrained boundary condition. The value at the injection point and the long-term limit is $\Delta\sigma_h/\Delta P = 0.58$ which is in agreement with the observed and empirical relationship for pore pressure/stress coupling. Figure 5 shows that pore pressure/stress coupling values are dependent on the distance of the observation point to the injection point and on the injection time. The empirical values or the observed values are the results for short distances to the injection points or long injection times. At shorter injection times there can be significant variations in the value of pore pressure/stress coupling.

In the inhomogeneous Model B we build an inner area representing a reservoir with a 100 times higher permeability than that of the surroundings (Figure 3(b)) and consider longer injection times. This model geometry results in increased stress and pore pressure inside the reservoir, compared to the results of the homogeneous Model A for the same injection times (Figures 6 and 7). This behaviour results from the decreased permeability of the surroundings, which leads to lesser fluid flow from the reservoir into the surroundings, and therefore to an accumulation of fluid inside the reservoir, compared to the modelling results with homogeneous permeability distribution. The additional fluid inside the reservoir increases the pore pressure, whereas in the surroundings, the stress increases strongly. The pore pressure/stress coupling $\Delta\sigma_h/\Delta P$ for the inhomogeneous Model B is shown in Figure 7. There is a reduction of $\Delta\sigma_h/\Delta P$ within the reservoir in comparison to the values of the homogeneous model and a very strong increase of pore pressure/stress coupling directly outside the reservoir. This increase of pore pressure/stress coupling mainly results from the strong decrease of the pore pressure at the reservoir boundary.

In summary, the calculated pore pressure/stress coupling $\Delta\sigma_h/\Delta P$ values based on the quasi-static poroelasticity approach and thus, based on the spatial-temporal distribution of P and the stress tensor, show a strong dependence on injection time and distance to the injection point. Only for long injection times will the observed $\Delta\sigma_h/\Delta P$ values approach the static solution.

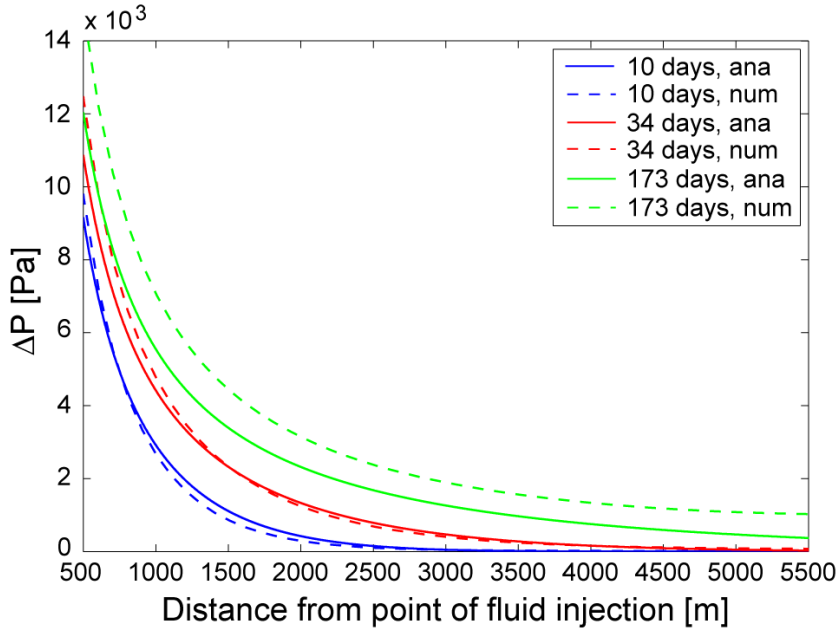

Figure 4 **Analytical and numerical computations of the spatial-temporal variation of pore pressure P for Model A**

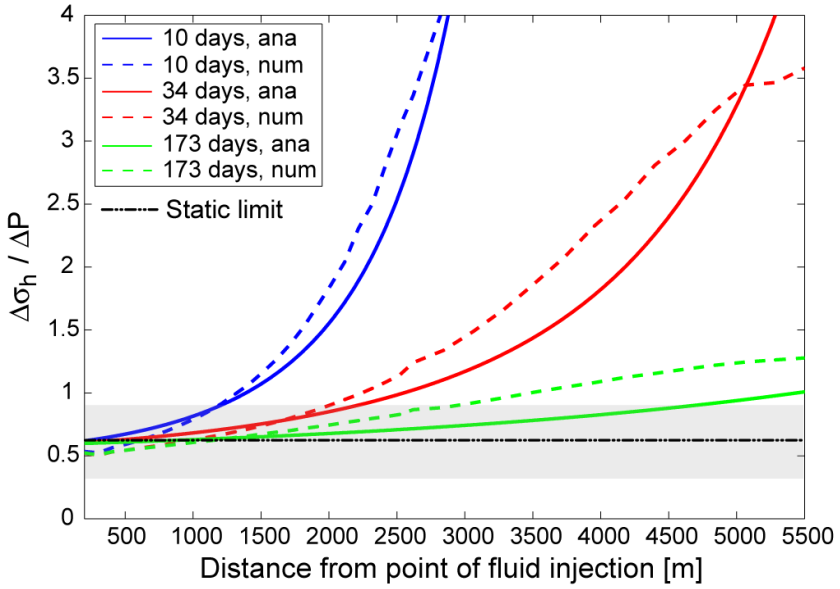

Figure 5 **Pore pressure/stress coupling ratio $\Delta\sigma_h/\Delta P$ for model A. The shaded area denotes the range of observed pore pressure/stress coupling values**

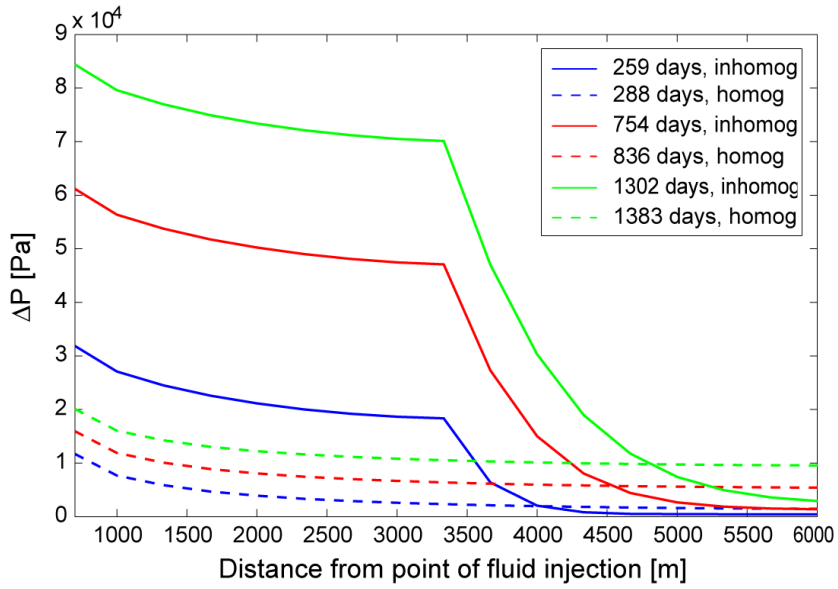

Figure 6 Comparison of numerical computations of the spatial-temporal variations of pore pressure P between homogeneous Model A and inhomogeneous Model B

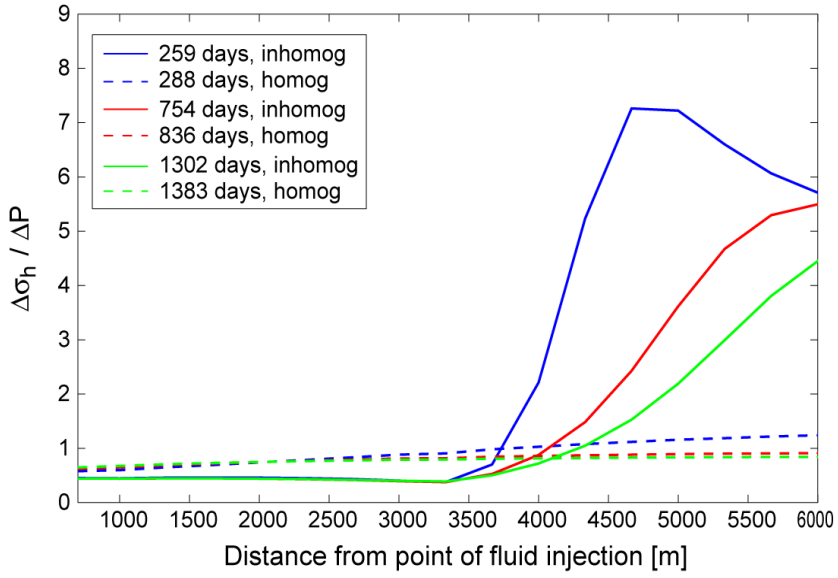

Figure 7 Comparison of numerical computations of the spatial-temporal variation of $\Delta\sigma_h/\Delta P$ between homogeneous Model A and inhomogeneous Model B

5 Conclusion

We conclude that pore pressure/stress coupling is not a constant value throughout the lifetime of a reservoir and varies within the reservoir. We could show analytically that the uniaxial strain approach of (Engelder and Fischer, 1994) can be deduced as the static limit of the poroelastic equations. Our modelling results indicate that the pore pressure/stress coupling deviates at reservoir scale from the elastic limit, in particular during the first several months of injection. Only in the near field and for long injection times the numerical solution converges towards the static limit. Our exemplary studies have shown a) that finite element modelling is a reliable tool to model coupled poroelastic effects and b) the importance of the reservoir size and the permeability changes at the reservoir boundaries. The results of the inhomogeneous model indicate that the reservoir size and shape as well as reservoir properties may control the distribution of P and stress and thus pore pressure/stress coupling. However, more quantitative results in a more systematic approach are

needed. Using numerical modelling the pore pressure effects on the maximum horizontal stress and the vertical stress also can be determined.

To predict the distribution of induced microseismicity the current approach is to use pore pressure distribution in combination with a criticality field (Shapiro et al., 2002). The poroelastic finite-element modelling of our study enables the calculation of P, normal stress σ_n and shear stress τ as a function of time for any location. As a consequence, these values can be included in a failure criterion for shear and tensile to predict the spatial-temporal distribution of failure planes either for fracturing or for reactivation of pre-existing fractures (Rozhko et al., 2007). In combination with numerical modelling, the spatial extent and onset of microseismicity in reservoirs can be deduced as function of reservoir properties (shape, volume, permeability, depletion rate) and tectonic setting.

Acknowledgements

This research has been supported by the Heidelberg Academy of Sciences and Humanities and the sponsors of the consortium project PHASE, the Deutsche Forschungsgemeinschaft (MU1725/1-3).

References

Addis, M.A. (1997) The stress-depletion response of reservoirs, SPE 38720, pp. 55–61.

Bell, J.S. (1990) The stress regime of the Scotian Shelf offshore eastern Canada to 6 kilometers depth and implications for rock mechanics and hydrocarbon migration. Rock at Great Depth, V. Maury and D. Fourmaintraux (editors), Balkema, Rotterdam, pp. 1243–1265.

Breckels, I.M. and van Eekelen, H.A.M. (1982) Relationship between horizontal stress and depth in sedimentary basins, Journal of Petroleum Technology, Vol. 34, pp. 2191–2198.

Doser, D.I., Baker, M.R., Luo, M., Marroquin, P., Bellesteros, L., Kingwell, J., Diaz, H.L. and Kaip, G. (1992) The not so simple relationship between seismicity and oil production in the Permian basin, West Texas, Pure and Applied Geophysics (Pageoph), Vol. 139, Birkhäuser Verlag, pp. 481–506.

Dost, B. and Haak, H. (2007) Natural and Induced Seismicity, Geology of the Netherlands, Royal Netherlands Academy of Arts and Sciences, pp. 223–239.

Engelder, T. and Fischer, M.P. (1994) Influence of poroelastic behavior on the magnitude of minimum horizontal stress, Sh in overpressured parts of sedimentary basins, Geology, Vol. 22, pp. 949–952.

Ervine, W.B. and Bell, J.S. (1987) Subsurface in situ stress magnitudes from oil-well drilling records: an example from the Venture area, offshore eastern Canada, Canadian Journal of Earth Sciences, Vol. 24, pp. 1748–1759.

Feigner, B. and Grasso, J.R. (1990) Seismicity Induced by Gas production: I Correlation of Focal Mechanisms and Dome Structure, Pure and Applied Geophysics (Pageoph), Vol. 134, Birkhäuser, pp. 405–426.

Geertsma, J. (1973) A basic theory of subsidence due to reservoir compaction: the homogeneous case, Nederland Geologie Mijnbouw, Vol. 28, pp. 43–62.

Grasso, J.R. (1992) Mechanics of Seismic Instabilities Induced by the Recovery of Hydrocarbons, Pure and Applied Geophysics (Pageoph), Vol. 139, Birkhäuser, pp. 507–534.

Grasso, J.R. and Wittlinger, G. (1990) Ten Years of Seismic Monitoring Over a Gas Field, Bulletin of the Seismological Society of America, Vol. 80, pp. 450–473.

Hillis, R.R. (2000) Pore pressure/stress coupling and its implications for seismicity, Exploration Geophysics, Vol. 31, pp. 448–454.

Hillis, R.R. (2001) Coupled changes in pore pressure and stress in oil fields and sedimentary basins. Petroleum Geoscience, Vol. 7, pp. 419–425.

Hillis, R.R. (2003) Pore pressure/stress coupling and its implications for rock failure. Subsurface Sediment Mobilization, P. Vanrensbergen, R.R. Hillis, A.J. Maltman and C.K. Morley (editors), Geological Society, London, pp. 359–368.

Jaeger, J.C. and Cook, N.G.W. (1979) Fundamentals of Rock Mechanics, Chapman and Hall, p. 475.

McGarr, A. (1982) Analysis of states of stress between provinces of constant stress, Journal of Geophysical Research, Vol. 87(B11), pp. 9279–9288.

Mereu, R.F., Brunet, R.F., Morrissey, K., Price, B. and Yapp, A. (1986) A study of the microearthquakes of the Gobles oil area of Southwestern Ontario, Bulletin of the Seismological Society of America, Vol. 76, pp. 1215–1223.

Mulders, F.M.M. (2003) Modelling of stress development and fault slip in and around a producing gas reservoir, Delft, 272 p.

Nicholson, C. and Wesson, R.L. (1992) Triggered Earthquakes and Deep Well Activities, Pure and Applied Geophysics (Pageoph), Vol. 139, Birkhäuser Verlag, pp. 561–578.

Roest, J.P.A., Mulders, F.M.M. and Kuilman, W. (1999) Data-limited geomechanical modelling for investigating induced seismicity mechanisms, ISRM–Congress, Paris, p. 5.

Rozhko, A.Y., Podladchikov, Y.Y. and Renard, F. (2007) Failure patterns caused by localized rise in pore-fluid overpressure and effective strength of rocks, Geophysical Research Letters, Vol. 34, p. 5.

Rudnicki, J.W. (1986) Fluid Mass Sources and Point Forces in Linear Elastic Diffusive Solids, Mechanics of Materials, Vol. 5, Elsevier, pp. 383–393.

Rutledge, J.T., Phillips, W.S. and Schuessler, B.K. (1998) Reservoir characterization using oil-production-induced microseismicity, Clinton County, Kentucky, Tectonophysics, Vol. 289, Elsevier, pp. 129–152.

Salz, L.B. (1977) Relationship between fracture propagation pressure and pore pressure, SPE 52nd Annual conference, Denver, Colorado, p. 8.

Segall, P. (1992) Induced stresses due to fluid extraction from axisymmetric reservoirs, Pure and Applied Geophysics (Pageoph), Vol. 139, pp. 535–560.

Simpson, R.W. and Leith, W. (1985) The 1976 and 1984 Gazli, USSR, earthquakes – were they induced? Seismological Society of America Bulletin, Vol. 75, pp. 1465–1468.

Shapiro, S.A., Rothert, E., Rath, V. and Rindschwentner, J. (2002) Characterization of fluid transport properties of reservoirs using induced microseismicity, Geophysics, Vol. 67, Society of Exploration Geophysicists, pp. 212–220.

Sze, E., Toksöz, M.N. and Burns, D.R. (2005) Characterization of Induced Seismicity in a Petroleum Reservoir: A Case Study, MIT, p. 7.

Teufel, L.W., Rhett, D.W. and Farrell, H.E. (1991) Effect of reservoir depletion and pore pressure drawdown on in situ stress and deformation in the Ekofisk field, North Sea, Rock Mechanics as a Multidisciplinary Science, J-C. Rogiers (editor), Balkema, Rotterdam, pp. 63–72.

Teufel, L.W. (1996) Influence of Pore pressure and production-induced Changes in Pore Pressure on In Situ Stress, U.S. Department of Energy Report, p. 54.

Tingay, M.R.P., Hillis, R.R., Morley, C.K., Swarbrick, R.E. and Okpere, E.C. (2003) Pore pressure/stress coupling in Brunei Darussalam – implications for shale injection, Subsurface Sediment Mobilization, P.V. Rensbergen, R.R. Hillis, A.J. Maltman and C.K. Morley (editors), Geological Society, London, pp. 369–379.

van Eck, T., Goutbeek, F., Haak, H. and Dost, B. (2006) Seismic hazard due to small-magnitude, shallow-source induced earthquakes in The Netherlands, Engineering Geology, Vol. 87, Elsevier, pp. 105–121.

van Eijs, R.M.H.E., Mulders, F.M.M., Nepveu, M., Kenter, C.J. and Scheffers, B.C. (2006) Correlation between hydrocarbon reservoir properties and induced seismicity in the Netherlands, Engineering Geology, Vol. 84, Elsevier, pp. 99–111.

Wang, H.F. (2000) Theory of linear poroelasticity with applications to geomechanics and hydrogeology, Princeton University Press, p. 276.

Yerkes, R.F. and Castle, R.O. (1976) Seismicity and Faulting Attributable to Fluid Extraction, Engineering Geology, Vol. 10, Elsevier, pp. 151–167.

Appendix — Derivation of limiting value for pore pressure/stress coupling ratios

To derive the limiting value for radial pore pressure/stress coupling ratios we apply the rules of L´Hospitales. If $F(x) = \varphi(x) \big/ \Psi(x)$ and the following limits hold:

$$\lim_{x \to a} \varphi(x) = 0 \quad \lim_{x \to a} \Psi(x) = 0 \tag{A-1}$$

then, it is also true that:

$$\lim_{x \to a} F(x) = \lim_{x \to a} \frac{\varphi(x)}{\Psi(x)} = \lim_{x \to a} \frac{\varphi'(x)}{\Psi'(x)} \tag{A-2}$$

accordingly, in order to evaluate:

$$\lim_{\xi \to 0} \frac{2 \cdot g(\xi)}{f(\xi)} \tag{A-3}$$

where:

$$\begin{aligned} g(\xi) &= \operatorname{erf}\left(\frac{1}{2}\xi\right) - \frac{1}{\sqrt{\pi}} \cdot \xi \cdot \exp\left(-\frac{1}{4}\xi^2\right). \\ f(\xi) &= \xi^2 \operatorname{erfc}\left(\frac{1}{2}\xi\right) \end{aligned} \tag{A-4}$$

We apply the rule (A-2) twice. Noting that the second derivatives are given by:

$$g''(\xi) = \frac{1}{\sqrt{\pi}}\left[\xi - \frac{1}{2}\xi^3\right] \cdot \exp\left(-\frac{1}{4}\xi^2\right) \tag{A-5}$$

$$f''(\xi) = 2\operatorname{erfc}\left(\frac{1}{2}\xi\right) + \left[\frac{1}{\sqrt{\pi}}\xi^3 - \frac{8}{\sqrt{\pi}}\xi\right] \cdot \exp\left(-\frac{1}{4}\xi^2\right)$$

we find:

$$\lim_{\xi \to 0} g''(\xi) = 0 \qquad \text{and} \qquad \lim_{\xi \to 0} f''(\xi) = 2 \tag{A-6}$$

where we used:

$$\lim_{\xi \to 0} \operatorname{erfc}(\xi) = 1 \tag{A-7}$$

therefore:

$$\lim_{\xi \to 0} \frac{2 \cdot g(\xi)}{f(\xi)} = \lim_{\xi \to 0} \frac{2 \cdot g''(\xi)}{f''(\xi)} = 0\,. \tag{A-8}$$